

Single-particle cryo-EM at atomic resolution

<https://doi.org/10.1038/s41586-020-2829-0>

Received: 22 May 2020

Accepted: 27 August 2020

Published online: 21 October 2020

 Check for updates

Takanori Nakane^{1,9}, Abhay Kotecha^{2,9}, Andrija Sente^{1,9}, Greg McMullan¹, Simona Masiulis^{1,7}, Patricia M. G. E. Brown¹, Ioana T. Grigoras^{1,8}, Lina Malinauskaitė¹, Tomas Malinauskas³, Jonas Miehling¹, Tomasz Uchański^{4,5}, Lingbo Yu², Dimple Karia², Evgeniya V. Pechnikova², Erwin de Jong², Jeroen Keizer², Maarten Bischoff², Jamie McCormack², Peter Tiemeijer², Steven W. Hardwick⁶, Dimitri Y. Chirgadze⁶, Garib Murshudov¹, A. Radu Aricescu^{1,8} & Sjors H. W. Scheres^{1,2}

The three-dimensional positions of atoms in protein molecules define their structure and their roles in biological processes. The more precisely atomic coordinates are determined, the more chemical information can be derived and the more mechanistic insights into protein function may be inferred. Electron cryo-microscopy (cryo-EM) single-particle analysis has yielded protein structures with increasing levels of detail in recent years^{1,2}. However, it has proved difficult to obtain cryo-EM reconstructions with sufficient resolution to visualize individual atoms in proteins. Here we use a new electron source, energy filter and camera to obtain a 1.7 Å resolution cryo-EM reconstruction for a human membrane protein, the β3 GABA_A receptor homopentamer³. Such maps allow a detailed understanding of small-molecule coordination, visualization of solvent molecules and alternative conformations for multiple amino acids, and unambiguous building of ordered acidic side chains and glycans. Applied to mouse apoferritin, our strategy led to a 1.22 Å resolution reconstruction that offers a genuine atomic-resolution view of a protein molecule using single-particle cryo-EM. Moreover, the scattering potential from many hydrogen atoms can be visualized in difference maps, allowing a direct analysis of hydrogen-bonding networks. Our technological advances, combined with further approaches to accelerate data acquisition and improve sample quality, provide a route towards routine application of cryo-EM in high-throughput screening of small molecule modulators and structure-based drug discovery.

Multiple factors determine the attainable resolution of reconstructions from single-particle cryo-EM. However, for biological macromolecules, the radiation damage caused by electron interactions with the sample is a fundamental limitation. To preserve the molecular structure, damage is restricted by carefully limiting the number of electrons used for imaging⁴. The resulting counting statistics lead to high levels of noise. The signal-to-noise ratio (SNR) of cryo-EM images drops rapidly with spatial frequency, and at higher spatial frequencies the noise is typically orders of magnitude higher than the signal.

High-resolution reconstructions can still be calculated by averaging over many images of individual particles, provided that their relative orientations can be determined. However, because noise reduction scales with the square root of the number of particles, and because higher SNRs lead to more accurate orientations, acquiring more particles is often less efficient than increasing the SNR in the images. Consequently, although microscope automation⁵ and faster image processing programs^{6,7} have allowed reconstructions from larger datasets in recent years, increasing the SNR of the raw data may lead to bigger improvements, as is illustrated by the sudden increase in

cryo-EM resolutions with the introduction of more sensitive direct electron cameras in 2013^{8,9}.

Here we describe the effect of three technological developments that further increase the SNR of cryo-EM images: a new cold field emission electron gun (CFEG), a new energy filter and the latest generation Falcon direct electron camera (Fig. 1a). Combined, these developments lead to a marked increase in the achievable resolution that ultimately enables the visualization of individual protein atoms in optimized samples.

Electron source optimized for energy spread

The source inside the microscope emits electrons with a range of different wavelengths, or energies. Because not all of these electrons can be focused in the same plane owing to chromatic aberration in the objective lens, the energy spread of the electrons leads to a blur in the images. The corresponding loss in SNR increases with spatial frequency and is described by an envelope on the contrast transfer function (CTF). Many state-of-the-art electron microscopes are equipped with a field emission gun (FEG) that is operated at a temperature of 1,700–1,800 K

¹MRC Laboratory of Molecular Biology, Cambridge, UK. ²Materials and Structural Analysis Division, Thermo Fisher Scientific, Eindhoven, The Netherlands. ³Division of Structural Biology, Wellcome Centre for Human Genetics, University of Oxford, Oxford, UK. ⁴Structural Biology Brussels, Vrije Universiteit Brussel, Brussels, Belgium. ⁵VIB-VUB Center for Structural Biology, VIB, Brussels, Belgium. ⁶Department of Biochemistry, University of Cambridge, Cambridge, UK. ⁷Present address: Materials and Structural Analysis Division, Thermo Fisher Scientific, Eindhoven, The Netherlands. ⁸Present address: Department of Physics, Imperial College London, London, UK. ⁹These authors contributed equally: Takanori Nakane, Abhay Kotecha, Andrija Sente.

✉ e-mail: radu@mrc-lmb.cam.ac.uk; scheres@mrc-lmb.cam.ac.uk

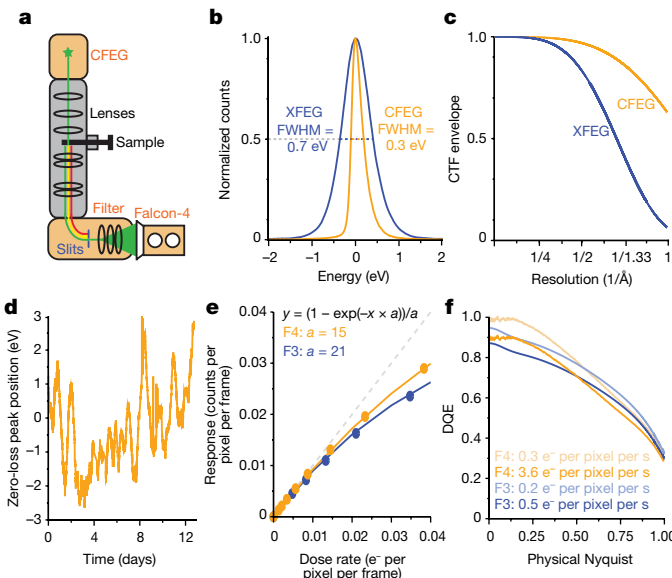


Fig. 1 | New imaging technologies for cryo-EM. **a**, Schematic overview of an electron cryo-microscope. The new CFEG, energy filter and Falcon-4 camera are coloured orange. **b**, Energy spread of the XFEG (blue) and CFEG (orange), with the full width of the curves at half their maximum value (FWHM). **c**, Theoretical CTF envelope functions for the XFEG (blue) and CFEG (orange). **d**, Relative position of the zero-loss peak with respect to the centre of the slits in the energy filter over multiple days of operation. **e**, Dose-response measurements for the Falcon-3 (F3; blue dots) and Falcon-4 (F4; orange dots). Orange and blue lines are corresponding fits to the data, with fit parameters indicated in the same colours; dashed grey line, perfect response. **x-axis units** are per camera frame, and the Falcon-4 and Falcon-3 operate at 248 and 40 frames per s, respectively. **f**, Detector Quantum Efficiency (DQE) curves for the Falcon-3 at dose rates of 0.2 (light blue) and 0.5 e⁻ per pixel per s (blue) and for the Falcon-4 at dose rates of 0.3 (light orange) and 3.6 e⁻ per pixel per s (orange).

and optimized for brightness (XFEG). To optimize the source for its energy spread, a so-called ‘cold’ FEG (CFEG) may be operated at room temperature instead. JEOL have pioneered the use of a CFEG for cryo-EM of biological macromolecules^{10,11}. We used a prototype of a CFEG that was recently developed by Thermo Fisher Scientific (TFS) and is operated at a low beam current. This reduces the brightness of the source from a typical $7.5 \times 10^7 \text{ A m}^{-2} \text{ sr}^{-1} \text{ V}^{-1}$ for a standard TFS XFEG to $5 \times 10^7 \text{ A m}^{-2} \text{ sr}^{-1} \text{ V}^{-1}$ for the CFEG at the beam current used for our experiments. However, compared to an energy spread of 0.7 eV for the XFEG, the new CFEG has an energy spread of 0.3 eV (Fig. 1b). As a result, the SNR increases at high spatial frequencies. Whereas the differences are small for resolutions worse than 2 Å, the use of the CFEG boosts the CTF from 58% to 91% at 1.5 Å, and from 26% to 80% at 1.2 Å. As the SNR scales with the square of the CTF, this leads to a 2.5-fold increase in the SNR at 1.5 Å and a 9.5-fold increase at 1.2 Å (Fig. 1c, Methods).

A disadvantage of operating the FEG at room temperature is that gas atoms can absorb to the surface of its tip, which reduces the number of electrons emitted. This contamination builds up over time and can be removed by periodically heating the tip. This procedure is called tip flashing and takes less than a minute. By performing tip flashing every 6–10 h, based on automated monitoring of the beam current in the data acquisition program EPU, we found that the CFEG beam current remained stable over days (Extended Data Fig. 1).

A stable energy filter

When electrons pass through the specimen, two types of interaction occur. Elastically scattered electrons maintain their energy and contribute to the signal in the images. Inelastically scattered electrons deposit part of their energy in the sample and contribute noise to the images.

Therefore, SNRs can be improved by filtering away electrons that have experienced an energy loss. Gatan pioneered the use of energy filters with a 90° bending prism for biological cryo-EM, and their filters are in widespread use¹². JEOL microscopes use a different, omega-shaped filter design¹³. We used a new energy filter developed by TFS using the experience that previously led to the energy filter described by Kahl et al.¹⁴. The filter is located below the projector column of the microscope and comprises a 90° bending prism with an adjustable energy-selecting slit and multiple electromagnetic lenses to correct for aberrations and to enlarge both the energy dispersion and the image. The mechanics of the new filter were designed to minimize the effect of temperature variations on the position of the optical elements, including the energy slit, with respect to the optical axis of the system. The large radius of the bending prism (135 mm compared to 75 mm in Gatan filters) reduces third- and fourth-order distortions. The new filter is stable over many days of operation: the position of the electrons that have not lost any energy, the so-called zero-loss peak, with respect to the centre of the energy slit changes by less than 3 eV in either direction (Fig. 1d).

A next-generation camera

The relatively large pixel size of Falcon direct-electron cameras, each measuring $14 \times 14 \mu\text{m}^{15}$, permits the use of a thick epilayer that increases the SNR^{16,17}. Noise in the resulting images arises mainly from the variation in height and shape of the charge distribution that is generated by individual incident electrons, or events. This noise can be reduced by a counting algorithm that positions a constant signal distribution at an estimated centre position for each event. However, in order to identify all individual events, the number of events that are in close proximity to each other on a single frame should be minimized. With a frame rate of 40 Hz, the Falcon-3 was the first Falcon camera that was fast enough for electron counting, but only when the electron dose was spread over typical exposure times of close to a minute.

The Falcon-4 camera operates at 248 Hz, while an improved counting algorithm estimates event positions with sub-pixel accuracy and its epilayer design optimizes the event size versus event signal strength and thereby reduces the number of events that are lost during counting (Fig. 1e). As a result, images with typical exposure times of a few seconds can be recorded, while the detective quantum efficiency remains similar to that of the Falcon-3 camera in counting mode (Fig. 1f). In addition, the resulting videos can be written out in a new data format, called electron-event representation (EER)¹⁸, which stores each detected electron event as an *x*, *y* position on a four-times oversampled grid and its original time, or frame, of recording. We adapted our image processing software RELION¹⁹ (see Methods) to read the new data format, thus allowing motion correction by the Bayesian polishing algorithm²⁰ and reconstructions of video frames with flexible dose fractionation schemes, up to the original frame rate of the camera.

Application to a human GABA_A receptor sample

To evaluate the effect of the technological advances described above, we used a homopentameric β3 γ-aminobutyric acid type-A receptor (GABA_AR) variant, an approximately 200-kDa human membrane protein bound to the Mb25 megabody to overcome its severe preferential orientation in ice^{3,21}. GABA_ARs are a large family of pentameric ligand-gated chloride channels that mediate inhibitory neurotransmission and are targeted by a wide range of psychoactive drugs²². However, structure-based drug development has been hampered by the difficulty of solving GABA_AR structures, which are currently limited to 2.5–3 Å resolution in the best cases^{21,23}. Whereas most GABA_ARs are heteromeric, β3-subunits form functional homomeric channels that are gated by histamine. Their fivefold symmetry allowed us to collect multiple datasets in a time-efficient manner, as one would need five times more data to reach the same resolution with an asymmetrical sample.

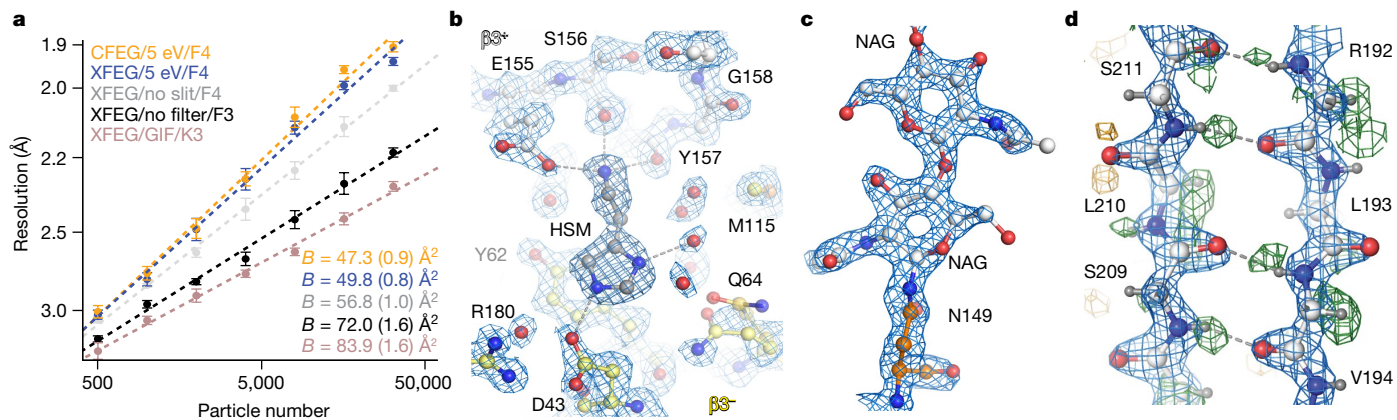


Fig. 2 | GABA_AR reconstructions. **a**, B-factor plots for five datasets using: the new CFEG, the new energy filter with a slit width of 5 eV and a Falcon-4 camera (orange); an XFEG, the new energy filter with a slit width of 5 eV and a Falcon-4 (blue); an XFEG, the new energy filter with the slits retracted and a Falcon-4 (grey); an XFEG, no energy filter and a (bottom-mounted) Falcon-3 detector (black); and an XFEG, a Gatan imaging filter (GIF) and a K3 detector (brown). B-factors estimated from the slopes of fitted straight lines are shown in the

same colours. Numbers in parentheses and error bars represent estimated and sample s.d.s from sevenfold random resampling, respectively. **b**, Overview of map quality at the agonist binding pocket, illustrating histamine (HSM) coordination and multiple water molecules (red spheres). **c**, The N-acetyl glucosamine (NAG) moieties attached to Asn149. **d**, Difference map (green, positive; orange, negative) visualizes hydrogen atoms in the hydrogen-bonding network between β-strands.

We collected seven datasets from three different GABA_AR grids on three different Titan Krios microscopes (Extended Data Table 1, Extended Data Fig. 2) and assessed their quality in terms of their estimated B-factors²⁴ (see Methods, Fig. 2a). To assess the current state of the art, we collected two datasets on a first grid on a microscope with an XFEG using either a Gatan K3 camera and a Gatan energy filter (with a slit width of 20 eV), or a bottom-mounted Falcon-3 camera. This resulted in B-factors of 84 and 72 Å², respectively. We note that data acquisition on the K3 was three times faster than on the Falcon-3. Therefore, reconstructions at a given target resolution may be obtained in less time on the K3. When we imaged a second grid on a microscope with an XFEG, the new energy filter (with retracted slits) and a Falcon-4 camera, an improvement of 15 Å² in the B-factor over the Falcon-3 dataset was observed. Using the same grid and the same microscope, a further improvement of 7 Å² in the B-factor was achieved when we used the energy filter with a slit width of 5 eV. Varying the energy slit widths to 3 eV and 10 eV did not have a noticeable effect on the B-factors (Extended Data Fig. 2a). Imaging a third grid on yet another microscope, with a CFEG, the new energy filter (with a slit width of 5 eV) and a Falcon-4 camera, led to a small improvement for those reconstructions with resolutions better than 2 Å. The latter is expected from the relatively small gains in the CTF envelope at those resolutions when using a CFEG instead of an XFEG (Fig. 1c). Finally, we performed tomography on the same GABA_AR grid used in the CFEG experiment to determine its ice thickness, which we found to be in the range of 320–370 Å (Extended Data Fig. 2b).

By combining the datasets with the new filter on both the XFEG and the CFEG, we obtained a 1.7 Å resolution reconstruction from 371,693 particles (Fig. 2b–d, Extended Data Figs. 2c–g, 3, Extended Data Table 2). The resulting map provides unprecedented levels of detail for a protein structure, other than apoferritin, solved by single-particle cryo-EM. The N-linked glycan on Asn149 shows density of exceptional quality; alternative side-chain conformations are visible for many amino acids; lipid molecules are visible in the transmembrane region of the receptor; and in the most ordered regions, hydrogen-bonding networks can be visualized directly in difference maps calculated in REFMAC²⁵ with a refined model from which the hydrogen atoms were omitted. Each agonist pocket is occupied by a histamine molecule, which binds in a similar manner to that observed for benzamidine³ and the neurotransmitter GABA²³. However, it is now possible to visualize the coordinating carboxyl groups of Glu155 and Asp43, alongside a network of ordered water molecules that surround the ligands to fill the agonist pocket.

A video of the dose-dependent evolution of the cryo-EM density indicates that the structure of the agonist pocket may be affected by radiation damage (Supplementary Video 1). Similarly, the disulfide bond between Cys136 and Cys150, a signature of the Cys-loop receptor family to which GABA_AR belongs, appears to be partially reduced during the electron exposure (Supplementary Video 2).

Atomic-resolution structure of apoferritin

To explore the potential of the new technologies to yield even higher-resolution reconstructions, we tested a mouse apoferritin sample. Apoferritin is a popular cryo-EM benchmark because its molecular stability and its 24-fold symmetry allow high-resolution reconstructions to be calculated from relatively few particles. Using JEOL's CFEG and omega energy filter with a K2 camera and the same mouse apoferritin sample as we use here, but a different grid, resulted in the best apoferritin map reported thus far, to our knowledge: 1.53 Å resolution from 120,295 particles, with a B-factor of 46 Å²¹¹. We previously also reported a reconstruction of human apoferritin with a resolution of 1.65 Å from 426,450 particles recorded on a Titan Krios microscope with an XFEG, a Gatan energy filter and a Gatan K2 camera¹⁹. The B-factor for that dataset was 66 Å².

We imaged mouse apoferritin on the CFEG microscope, using the Falcon-4 camera and a slit width of 10 eV in the new energy filter. From 3,370 videos, we obtained a reconstruction with a resolution of 1.22 Å from 363,126 particles (Extended Data Fig. 4, Supplementary Video 3). Corrections during image processing, for third and fourth-order optical aberrations²⁶, as well as for the curvature of the Ewald sphere^{19,27}, were crucial in obtaining a B-factor of 32 Å² (Fig. 3a). After sharpening of the map, most atoms are resolved as individual blobs of density; C=O bonds and some of the C–N bonds in the peptide planes are less well separated (Fig. 3b–d). Many hydrogen atoms, including those from individual water molecules, are resolved in a REFMAC difference map, more clearly than in the case of the GABA_A receptor and allowing a direct analysis of hydrogen-bonding networks (Fig. 3e, f). Detailed analysis of the hydrogen positions revealed that the density peaks in the difference map were consistently further from their bonded atom than the hydrogen atoms at its expected position. This result is explained by the observation that electron imaging visualizes electrostatic potential, which depends on the positions of both nuclei and electrons (see Methods, Extended Data Fig. 5).

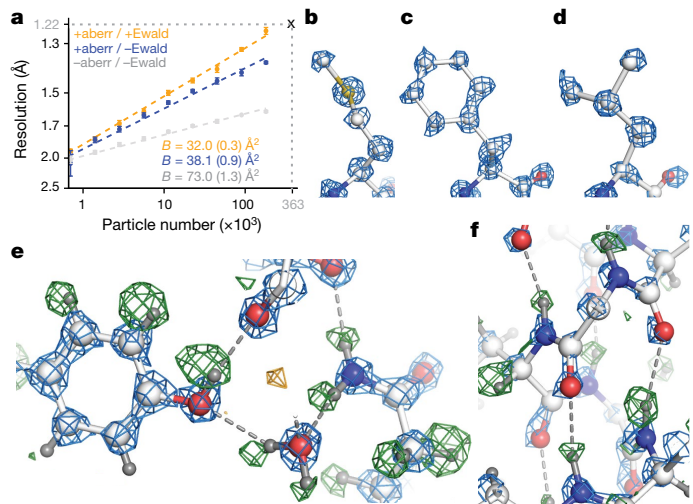


Fig. 3 | Apoferritin reconstruction. **a**, B-factor plots for reconstructions using: high-order aberration (+aberr) and Ewald sphere correction (+Ewald); high-order aberration correction only (blue); and no correction (grey). B-factors estimated from the slopes of fitted straight lines are shown in the same colours. Numbers in parentheses and error bars represent estimated and sample s.d.s from sevenfold random resampling, respectively. **b–d**, Densities from the 1.22 Å map (blue) for M100 (**b**), F51 (**c**) and L175 (**d**). **e**, Hydrogen-bonding network around Y32 and water-302 is visible in the difference map (green, positive; orange, negative). **f**, The α -helix hydrogen-bonding network involving residues $^{21}\text{NRQIN}^{25}$, shown as in **e**.

Finally, we calculated reconstructions for each of the 434 camera frames that were acquired per exposure and were able to follow the dose-dependent evolution of the cryo-EM density with an unprecedented resolution of 0.1 electrons (e^-) per \AA^2 (Supplementary Video 4). Following the initial dose of $1.5 \text{ e}^- \text{\AA}^{-2}$, the resolution of the single-frame reconstructions extended to 1.7 Å and remained better than 2 Å up to an accumulated dose of $11.5 \text{ e}^- \text{\AA}^{-2}$. However, the first few reconstructions were of relatively poor quality, probably because initial beam-induced motions were not modelled adequately. As radiation damage is minimal in the earliest frames, further improvements in beam-induced motion correction, possibly by considering particle rotations and height changes²⁸, may therefore extend the attainable resolution even further.

Outlook

The three developments in electron microscopy hardware described in this paper provide a step-change in the resolution that can be achieved using single-particle cryo-EM. Using apoferritin, we have shown that these developments allow the determination of the structure of a protein to true atomic resolution, as per the Sheldrick criterion^{29,30}. The improved energy spread of the CFEG is crucial for extending resolutions to better than 1.5 Å, consistent with similar observations made with the JEOL CFEG¹⁰. There are two alternatives to the CFEG strategy to improve the CTF envelope function at atomic resolution. First, one could use objective lenses with a lower chromatic aberration, which are common in material science, although their narrow gap polepieces would limit the amount by which the sample could be tilted. Second, one could reduce the energy spread by using a monochromator³¹. The disadvantage of this strategy would be a considerably more complicated experimental setup.

Our results for the GABA_AR illustrate how the new technology can improve cryo-EM structures at lower resolutions, beyond the highly stable test samples that are represented by apoferritin. Although variations between microscopes and grids can complicate direct comparisons of B-factors, our results for the GABA_AR suggest that the

Falcon-4 camera in combination with the new filter provides the best image quality (Fig. 2a). At this stage, it is unclear whether the removal of inelastically scattered electrons from our thin samples alone would be enough to account for this improvement, or whether other effects—for example, increased amplitude contrast³²—are also involved. In the future, it will also be of interest to explore whether, instead of removing them, inelastically scattered electrons could still be used to add to the signal in a chromatic-aberration-corrected microscope^{33,34}.

The increased SNR of cryo-EM images enabled by the technology described here will expand the applicability of both single-particle analysis and electron tomography to more difficult samples, including membrane proteins in lipid bilayers, small proteins and structurally heterogeneous macromolecular complexes. Moreover, higher-resolution reconstructions will allow improved visualization of hydrogen-bonding networks, ordered waters and alternative side-chain conformations, which will further our understanding of protein function and facilitate cryo-EM fragment-based drug discovery.

Online content

Any methods, additional references, Nature Research reporting summaries, source data, extended data, supplementary information, acknowledgements, peer review information; details of author contributions and competing interests; and statements of data and code availability are available at <https://doi.org/10.1038/s41586-020-2829-0>.

- Cheng, Y. Single-particle cryo-EM at crystallographic resolution. *Cell* **161**, 450–457 (2015).
- Lyumkis, D. Challenges and opportunities in cryo-EM single-particle analysis. *J. Biol. Chem.* **294**, 5181–5197 (2019).
- Miller, P. S. & Aricescu, A. R. Crystal structure of a human GABA_A receptor. *Nature* **512**, 270–275 (2014).
- Glaeser, R. M. Specimen behavior in the electron beam. *Methods Enzymol.* **579**, 19–50 (2016).
- Suloway, C. et al. Automated molecular microscopy: the new Leginon system. *J. Struct. Biol.* **151**, 41–60 (2005).
- Kimanis, D., Forsberg, B. O., Scheres, S. H. & Lindahl, E. Accelerated cryo-EM structure determination with parallelisation using GPUs in RELION-2. *eLife* **5**, e18722 (2016).
- Punjani, A., Rubinstein, J. L., Fleet, D. J. & Brubaker, M. A. cryoSPARC: algorithms for rapid unsupervised cryo-EM structure determination. *Nat. Methods* **14**, 290–296 (2017).
- McMullan, G., Faruqi, A. R., Clare, D. & Henderson, R. Comparison of optimal performance at 300 keV of three direct electron detectors for use in low dose electron microscopy. *Ultramicroscopy* **147**, 156–163 (2014).
- Kühlbrandt, W. The resolution revolution. *Science* **343**, 1443–1444 (2014).
- Hamaguchi, T. et al. A new cryo-EM system for single particle analysis. *J. Struct. Biol.* **207**, 40–48 (2019).
- Kato, T. et al. CryoTEM with a cold field emission gun that moves structural biology into a new stage. *Microsc. Microanal.* **25**, 998–999 (2019).
- Gubbens, A. et al. The GIF Quantum, a next generation post-column imaging energy filter. *Ultramicroscopy* **110**, 962–970 (2010).
- Tanaka, M. et al. A new 200 kV Ω -filter electron microscope. *J. Microscopy* **194**, 219–227 (1999).
- Kahl, F. et al. in *Advances in Imaging and Electron Physics* Vol. 212 (eds Hawkes, P. W. & Hÿtch, M.) 35–70 (Elsevier, 2019).
- Kuijper, M. et al. FEI's direct electron detector developments: Embarking on a revolution in cryo-TEM. *J. Struct. Biol.* **192**, 179–187 (2015).
- McMullan, G., Faruqi, A. R. & Henderson, R. Direct electron detectors. *Methods Enzymol.* **579**, 1–17 (2016).
- Ruskin, R. S., Yu, Z. & Grigorieff, N. Quantitative characterization of electron detectors for transmission electron microscopy. *J. Struct. Biol.* **184**, 385–393 (2013).
- Guo, H. et al. Electron event representation (EER) data enables efficient cryoEM file storage with full preservation of spatial and temporal resolution. *IUCrJ* **7**, 860–869 (2020).
- Zivanov, J. et al. New tools for automated high-resolution cryo-EM structure determination in RELION-3. *eLife* **7**, e42166 (2018).
- Zivanov, J., Nakane, T. & Scheres, S. H. W. A Bayesian approach to beam-induced motion correction in cryo-EM single-particle analysis. *IUCrJ* **6**, 5–17 (2019).
- Ucharński, T. et al. Megabodies expand the nanobody toolkit for protein structure determination by single-particle cryo-EM. Preprint at <https://doi.org/10.1101/812230> (2019).
- Sieghart, W. & Savić, M. M. International Union of Basic and Clinical Pharmacology. CVI: GABA_A receptor subtype- and function-selective ligands: key issues in translation to humans. *Pharmacol. Rev.* **70**, 836–878 (2018).
- Masiulis, S. et al. GABA_A receptor signalling mechanisms revealed by structural pharmacology. *Nature* **565**, 454–459 (2019).
- Rosenthal, P. B. & Henderson, R. Optimal determination of particle orientation, absolute hand, and contrast loss in single-particle electron cryomicroscopy. *J. Mol. Biol.* **333**, 721–745 (2003).

25. Nicholls, R. A., Tykac, M., Kovalevskiy, O. & Murshudov, G. N. Current approaches for the fitting and refinement of atomic models into cryo-EM maps using CCP-EM. *Acta Crystallogr. D* **74**, 492–505 (2018).
26. Zivanov, J., Nakane, T. & Scheres, S. H. W. Estimation of high-order aberrations and anisotropic magnification from cryo-EM data sets in RELION-3.1. *IUCrJ* **7**, 253–267 (2020).
27. Russo, C. J. & Henderson, R. Ewald sphere correction using a single side-band image processing algorithm. *Ultramicroscopy* **187**, 26–33 (2018).
28. Tegunov, D., Xue, L., Dienemann, C., Cramer, P. & Mahamid, J. Multi-particle cryo-EM refinement with M visualizes ribosome-antibiotic complex at 3.7 Å inside cells. Preprint at <https://doi.org/10.1101/2020.06.05.136341> (2020).
29. Sheldrick, G. Phase annealing in SHELX-90: direct methods for larger structures. *Acta Crystallogr. A* **46**, 467–473 (1990).
30. Wlodawer, A. & Dauter, Z. ‘Atomic resolution’: a badly abused term in structural biology. *Acta Crystallogr. D* **73**, 379–380 (2017).
31. Tiemeijer, P. C., Bischoff, M., Freitag, B. & Kisielowski, C. Using a monochromator to improve the resolution in TEM to below 0.5 Å. Part I: Creating highly coherent monochromated illumination. *Ultramicroscopy* **114**, 72–81 (2012).
32. Langmore, J. P. & Smith, M. F. Quantitative energy-filtered electron microscopy of biological molecules in ice. *Ultramicroscopy* **46**, 349–373 (1992).
33. Rose, H. H. Future trends in aberration-corrected electron microscopy. *Philos. Trans. A Math. Phys. Eng. Sci.* **367**, 3809–3823 (2009).
34. Haider, M., Hartel, P., Müller, H., Uhlemann, S. & Zach, J. Current and future aberration correctors for the improvement of resolution in electron microscopy. *Philos. Trans. A Math. Phys. Eng. Sci.* **367**, 3665–3682 (2009).

Publisher's note Springer Nature remains neutral with regard to jurisdictional claims in published maps and institutional affiliations.

© The Author(s), under exclusive licence to Springer Nature Limited 2020

Methods

Characterization of the new microscopy hardware

The energy spread of the field emission gun was measured using the new energy filter. Post-slit multi-poles of the filter were set to spectroscopy mode in order to form an enlarged image of the spectrum on the camera. The intensity of the incoming beam was carefully reduced so as not to saturate or damage the camera. The energy dispersion at the camera was 8 meV/pixel. The exposure time was 31 ms. The energy spread as FWHM of $\Delta E = 0.71$ for XFEG, and $\Delta E = 0.28$ for CFEG (Fig. 1b) were used to calculate the CTF envelope function, defocus spread Δf , using the following equation³¹:

$$\Delta f = C_c \sqrt{(\Delta E/eV)^2 + (\Delta V/V)^2 + (2\Delta I/I)^2},$$

using chromatic aberration constant $C_c = 2.7$ mm; gun energy spread $\Delta V/V = 0.02$ ppm and objective lens current instability $\Delta I/I = 0.1$ ppm. Note that the latter two contributions account for less than a 1% drop in the CTF envelope.

The stability of the energy filter was assessed by repeatedly measuring the position of the zero-loss peak with respect to the energy-selecting slit. To this end, we mechanically moved one slit edge to the optical axis and fine-tuned an offset on the high tension supply such that the slit edge blocked half of the beam intensity. The resulting offset of the high tension was read out as the shift in the zero loss position. Measurements, each taking approximately 40 s, were repeated continuously for 14 days.

Dose-response curves for the Falcon-3 and Falcon-4 cameras were measured using the flu-screen and fixed magnification steps. Before each experiment, the flu-screen was carefully calibrated with a Faraday cup in its linear range (0.4–5.0 nA at 300 kV). The read-out from the flu-screen was interpreted as the expected electron dose and plotted against the counted number of electrons on the camera.

DQE measurements were performed as described³⁵ at 300 keV on a Titan Krios G2 microscope at the LMB for the Falcon-3 and on a Titan Krios G3i microscope at the Materials Science Department of the University of Cambridge, UK for the Falcon-4. For calibration of the flu-screen on the microscope with the Falcon-4, a Faraday cage and a Keithley 6485 picoammeter (provided by G. van Hoften, Thermo Fisher Scientific) were used. For the microscope with the Falcon-3, the drift tube of a Gatan energy filter (BioQuantum 686) was used as a Faraday cup and the current was measured using a Deben 087-001 SEM probe current meter. Because the beam currents used in counting mode imaging are too low to be accurately measured, a defined beam with a measurable current was set at a low magnification and the desired electron flux on the camera was obtained by increasing the magnification. The relative magnification change was measured by using a higher current to fully illuminate the flu-screen at the low magnification and noting the change in current upon going to the higher magnification.

To account for the nonlinearity that is introduced by coincidence loss, DQEs were first measured at a low dose rate (0.19 e⁻/pixel/s for the Falcon-3; 0.32 e⁻/pixel/s for the Falcon-4) and then extrapolated to a typical dose rate (0.5 e⁻/pixel/s for the Falcon-3; 3.6 e⁻/pixel/s for the Falcon-4) using the measured response versus dose-rate curves (Fig. 1e). Modulation transfer functions (MTFs) were measured using the knife-edge method from a straight part of a shadow of the pointer on the camera. The actual area of the images used was chosen carefully by looking at the difference between the observed image and that predicted from the inferred MTF, to ensure that the edge in the selected area was straight and free of defects. In the case of the Falcon-4, the only part of the pointer edge that was suitable was at a 15° angle to the pixel array of the camera, the effect of which was accounted for when calculating the MTF. Even at the lowest dose rates used, there was still a small decrease in the power spectra at low spatial frequencies due to coincidence loss. To avoid overestimating the resulting DQE at low

spatial frequency, the noise power spectra were extrapolated from a Gaussian fit of the power between 0.2 and 0.8 of Nyquist. The amplitudes and widths of fitted Gaussians to the noise power spectra were in excellent agreement with those expected from the number of counted electrons per frame and estimates from the point spread functions of images of individual incident electrons.

GABA_A receptor production, purification and nanodisc reconstitution

Human GABA_A receptor β₃-subunit with a truncated M3–M4 loop was transiently expressed in HEK293S GnT⁻ cells (which lack N-acetylglucosaminyltransferase I activity) as previously described³. The sample used for XFEG datasets collected on a Falcon-4 contained a point mutation (K279T) that is thought to stabilize the receptor and a C-terminal 1D4 tag for purification. The sample used for the CFEG dataset, as well as the Falcon-3 and K3 datasets, contained the wild-type sequence and an N-terminal streptavidin-binding peptide (SBP) tag for purification. Subsequent comparison of the resulting cryo-EM maps revealed that the K279T mutation had no structural impact, so the Falcon-4 datasets could be merged during data processing. Frozen cell pellets were resuspended in 50 mM 4-(2-hydroxyethyl)-1-piperazineethanesulfonic acid (HEPES) pH 7.6, 300 mM NaCl, 1 mM histamine supplemented with 1% (v/v) mammalian protease inhibitor cocktail (Sigma-Aldrich) and solubilized with 1% (w/v) lauryl maltose neopentyl glycol (LMNG) and 0.1% (w/v) cholesterol hemisuccinate Tris salt (CHS). No CHS was added to the sample that was used for the CFEG dataset. Receptors were purified by 1D4 and SBP affinity chromatography. Nanodisc reconstitution was performed as previously described²³. In brief, after the binding step, while the receptor was still bound to the affinity beads, an excess of bovine brain extract (BBE; type I, Folch fraction I, Sigma-Aldrich, 20 mg/ml stock) and phosphatidylcholine (POPC, Avanti, 10 mg/ml) mixture (15:85, v/v) was added to the samples and incubated for 30 min. Receptors were then reconstituted into membrane scaffold protein 2N2 (MSP2N2) lipid nanodiscs by incubating with an excess of MSP2N2 (0.6 mg/ml final concentration) and bio-beads for 2 h. The resin was then washed extensively and the GABA_AR samples were eluted with a buffer containing 12.5 mM HEPES pH 7.6, 75 mM NaCl, 1 mM histamine and 2 mM 1D4 peptide or 2.5 mM biotin.

Cryo-EM grid preparation

Purified GABA_AR was incubated with -1 μM Megabody-25²¹ and a 3.5-μl sample was applied to glow-discharged 300 mesh 1.2/1.3 and 2/2 UltraAuFoil gold grids (Quantifoil) for 30 s then blotted for 5.5 s before plunge-freezing with liquid ethane cooled by liquid nitrogen. Grid vitrification was performed using a Leica plunger (Leica Microsystems; XFEG datasets) or Vitrobot Mark IV (Thermo Fisher Scientific; CFEG datasets) at 100% humidity and 14 °C.

A frozen aliquot of 7 mg/ml mouse apoferritin in 20 mM HEPES pH 7.5, 150 mM NaCl, 1 mM dithiothreitol (DTT) and 5% trehalose, which we received from the Kikkawa laboratory at Tokyo University, was thawed at room temperature and cleared by centrifugation at 10,000g for 10 min. The supernatant was diluted to 5 mg/ml with 20 mM HEPES pH 7.5 150 mM NaCl, and 3 μl of the diluted sample was applied onto glow-discharged R1.2/1.3 300 mesh UltraAuFoil gold grids (Quantifoil) for 30 s and then blotted for 5 s before plunge-freezing the grids into liquid ethane cooled by liquid nitrogen. Plunge-freezing was performed using a Vitrobot Mark IV (Thermo Fisher Scientific) at 100% humidity and 4 °C.

Cryo-EM data acquisition

All cryo-EM data were collected on Falcon or K3 cameras in electron counting mode using Titan Krios microscopes (Thermo Fisher Scientific) operating at 300 kV. Before data acquisition, twofold astigmatism was corrected and beam tilt was adjusted to the coma-free axis using the autoCTF program (Thermo Fisher Scientific). All datasets

Article

were acquired automatically using EPU software (Thermo Fisher Scientific). Detailed data acquisition parameters for all datasets are given in Extended Data Table 1.

For GABA_AR, two datasets were acquired on a Titan Krios at the Department of Biochemistry, University of Cambridge, UK. This microscope is equipped with an XFEG and a bottom-mounted (BM) Falcon-3 camera and a K3 camera behind the Gatan energy filter. All other datasets were acquired at the Thermo Fisher Scientific R&D division in Eindhoven, The Netherlands. Four GABA_AR datasets were collected on a Titan Krios equipped with an XFEG and a prototype Falcon-4 camera that was mounted behind the new energy filter. These datasets were collected consecutively over a period of five days from the same grid to study the effect of varying energy slit widths. To keep the ice thickness similar between these experiments, all the exposure areas were selected at the start using a constant ice filter within EPU software. One GABA_AR dataset was acquired on a microscope with a CFEG and a prototype Falcon-4 camera that was mounted behind the new energy filter. The slit width of the energy filter was set to 5 eV. For this dataset, 5,573 videos were acquired using a 100-μm objective aperture and 3,160 videos were collected without an objective aperture. The CFEG was automatically flashed every 5 h using the EPU software.

For the apoferritin dataset, we used the same microscope with the CFEG, the new filter and the prototype Falcon-4 camera. No objective aperture was used and the slit width of the energy filter was set to 10 eV. Flashing of the CFEG had no noticeable effect on data quality (Extended Data Fig. 4f).

Data acquisition was not optimized in terms of speed and the prototype Falcon-4 version did not write videos at the highest possible rate. Typically, two videos were collected per hole, with physical stage movements in between each hole. The resulting data acquisition rate was ~95 videos per hour (including Dewar filling times and CFEG flashing). The 3,370 apoferritin videos were collected within 36 h; GABA_AR datasets allowed ~2 Å reconstructions in ~9 h. Fringe free imaging (FFI) and aberration-free image shift (AFIS), which allow the acquisition of multiple images per hole and multiple holes per stage position, would allow considerably higher throughputs.

The EER movie format

Electron event representation (EER) is a video format that is introduced with the Falcon-4 camera¹⁸. Whereas in the existing MRC image format groups of subsequent camera frames, or dose fractions, are summed and represented as images, EER stores the location and time of recording of each detected electron event. The EER format records the event coordinates in a four times oversampled (16k × 16k) grid. The time resolution is the original frame rate of the camera, so that dose fractionation during data acquisition is no longer needed. Instead, beam-induced sample motions or stage drift can be corrected without a loss in temporal resolution. The electron event stream is stored on disk after compression with a run-length encoding algorithm. For GABA_AR, datasets were acquired at a dose rate of 4.7 electrons per pixel per second, at a pixel size of 0.727 Å and a total dose of 18.1 electrons per pixel. These settings yielded EER videos consisting of 1,113 frames and with an average size of 485 MB. For apoferritin, data were acquired at a dose rate of 4.5 electrons per pixel per second, at a pixel size of 0.457 Å and a total dose of 40 electrons per Å², resulting in videos of 434 frames occupying on average 160 MB.

To read EER movies, we modified the publicly available RELION-3.1-beta. Inside RELION, the events from the 16k × 16k grid are positioned as binary pixels in a 8k × 8k grid, which is then Fourier cropped into a 4k × 4k grid. Using the modified version, EER movies can be used for frame alignment using RELION's implementation of the MotionCor2 algorithm³⁶ and for per-particle beam-induced motion correction using its Bayesian polishing program²⁰. For both programs, the user needs to specify a dose fractionation rate.

Ice-thickness measurement

The ice thickness was measured on a GABA_AR grid using tomography. Tilt series were collected on three different grid-squares with a 10-eV slit on a Falcon-4 camera. Data were acquired covering an angular range from -45° to +45° with 3° angular increments recorded automatically using the dose-symmetric tilting scheme under low-dose conditions using TEM tomography software (TFS). Each tilt series was collected with a nominal defocus value of 5 μm in electron counting mode using a dose of 4 e⁻/Å² per tilt and a calibrated pixel size of 1.898 Å. Tomograms were reconstructed with patch tracking and ice thickness measured with IMOD software³⁷.

Apoferitin image processing

A total of 3,370 videos in EER format were motion corrected with RELION's implementation of the MotionCor2 algorithm³⁶. For this purpose, original hardware video frames were dose-fractionated into groups of 14 frames, corresponding to an accumulated dose of 1.3 e⁻/Å² per fraction. CTF estimation was performed with CTFFIND-4.1.13³⁸ using the sums of power spectra from combined fractions corresponding to an accumulated dose of 4 e⁻/Å². Micrographs whose estimated resolution from CTFFIND was worse than 5 Å were removed, leaving 3,080 micrographs for further processing.

Using RELION's template-based algorithm, 428,590 particles were picked and subjected to 2D classification. After selection of good classes, 380,236 particles were subjected to standard 3D auto-refinement to give an initial reconstruction with an estimated resolution of 2.3 Å. Subsequently, three runs of CTF refinement²⁶ were performed: first refining magnification anisotropy; then refining optical aberrations (up to the fourth order); and finally refining per-particle defocus and per-micrograph astigmatism. A 3D auto-refinement with the refined values yielded an estimated resolution of 1.7 Å. Bayesian polishing to optimise per-particle beam-induced motion tracks, followed by another round of auto-refinement, resulted in a 1.43 Å map. CTF refinement was then repeated for optical aberration correction, magnification anisotropy, per-particle defocus and per-micrograph astigmatism. To compensate for changes in the tilt of the electron beam during the data acquisition session, separate optics groups were created for particles belonging to consecutive groups of 125 micrographs, or whenever the CFEG was flashed. At this point, 201 micrographs with refined scale factors (rlnGroupScaleCorrection) with values below 0.5 were also removed, resulting in 363,126 particles in the final set (Extended Data Fig. 4f). Following a last round of auto-refinement, these particles were subjected to a second round of Bayesian polishing with a large particle extraction box (spanning 320 Å), such that high-resolution signals that were delocalized by the CTF were still contained in the images. At this point, seven hardware frames were grouped into each dose fraction to be able to capture more rapid motions. As Ewald sphere curvature was predicted to limit the resolution of a particle with a diameter of 120 Å to approximately 1.3 Å³⁹, the particles were then used for reconstruction with Ewald sphere correction²⁷. The estimated resolution of the final map, following standard post-processing procedures in RELION, was 1.22 Å.

GABA_A receptor image processing

GABA_AR datasets were processed following the same strategy as for apoferritin, with the following exceptions. All videos, except for those acquired on the microscope with a CFEG, were recorded in MRC format. For the CFEG data, hardware video frames were initially dose-fractionated into groups of 24 frames, corresponding to an accumulated dose of 0.86 e⁻/Å² per fraction. For the second round of Bayesian polishing, a dose fractionation of 12 hardware frames was used. Particle picking was performed using an in-house-generated Linux port of the BoxNet2D neural network in Warp⁴⁰. Prior to the last auto-refinement, 3D classification into three classes without alignment

was performed to select the particles contributing to the best reconstruction. The first part of the CFEG data was acquired with a 100- μm objective aperture. Charging of the aperture probably led to third- and fourth-order optical aberrations, which were estimated during CTF refinement in optics groups of 160 micrographs, or whenever the CFEG was flashed or liquid nitrogen was refilled. The second part of the CFEG data was acquired without an objective aperture. For these images, no significant higher-order optical aberrations were observed and creating multiple optics groups was deemed unnecessary. When merging the energy-filtered CFEG and XFEG datasets, refinement of per-micrograph scale factors and per-particle normalization corrections were unstable, and these were switched off using the `-no_norm` and `-no_scale` arguments. The mask used for resolution estimation during post-processing contained density for GABA_AR only; all density corresponding to the megabodies was removed.

B-factor estimation

For each GABA_AR dataset, a random subset of 32,000 particles was selected from the final set of particles after the second round of Bayesian polishing. This subset was subjected to 3D auto-refinement and the resulting orientations were used to calculate reconstructions for each of the two random halves used in the auto-refinement. Similar half-set reconstructions were also calculated for random subsets of 16,000, 8,000, 4,000, 2,000, 1,000 and 500 particles. This procedure was repeated seven times. For each subset and repeat, resolution estimation was again performed using standard post-processing functionality in RELION. The inverse square of the resulting estimated resolutions were then plotted against the natural logarithm of the number of particles in the subset, and *B*-factors were calculated from the slope of a straight line fitted through all points in the plot. For apoferritin, the same procedure was used, starting from a subset of 180,000 particles and halving the subset size eight times.

Atomic modelling

The atomic models for GABA_AR and apoferritin were derived from PDB-4cof and PDB-6s61, respectively. Both models were manually adjusted in COOT⁴¹. Difference maps were used to rebuild the model and to add alternative conformations and waters. Real-space refinement was performed using PHENIX, version 1.16.3549⁴² for GABA_AR. Both models were refined with anisotropic atomic *B*-factors in reciprocal space using REFMAC, version 5.8.0258²⁵. For cross-validation, the atomic models refined against the full map were perturbed by random shifts of the atoms of up to 0.3 Å and the perturbed model was refined in REFMAC against one of the two half-maps. FSC curves for the resulting model against that half-map (FSC_{work}) and against the other half-map (FSC_{free}) are shown with blue and dashed orange lines, respectively, in Extended Data Figs. 2, 4. Molprobity score, clash score, rotamer and Ramachandran analyses were performed using MOLPROBITY⁴³.

For refinement and difference map calculation, maps were first scaled globally using Gaussian scaling: that is, $\min_{k,B} \sum_k ||F_o - k e^{-Bs^2/4} |F_c||^2$, where *k* is the linear scale factor, *B* is the *B* factor, *s* = 1/*d* is the resolution, *F_o* is the Fourier transform of the post-processed map and *F_c* is the Fourier transform of a map calculated from a model without hydrogens. Next, each resolution shell was scaled by finding a scale factor *D* and sigma per shell with a maximum likelihood method: $\min_{D,\sigma} \sum_{D,\sigma} (|F_o - DF_c|^2/\sigma) + \sum \log(\sigma)$. Finally, difference maps were calculated as *F_o - DF_c*. As *F_o* is FSC weighted, the resulting map will be also FSC weighted. FSC is calculated from half maps. Structural figures were prepared using PyMOL (Schrödinger) and UCSF ChimeraX⁴⁴.

Hydrogen position calculations

X-ray scattering and electron scattering factors are related through the Mott–Bethe formula, which is the solution of Poisson equations in Fourier space under certain conditions:

$$f_e(s) = c \frac{Z - f_X(s)}{s^2}$$

Where $c = \frac{2\pi me^2}{h^2 \epsilon_0}$; *m* is the mass of an electron; *e* is the charge of an electron; *h* is the Planck constant; ϵ_0 is the dielectric constant of the vacuum; *Z* is the nuclear charge; *f_X(s)* is the X-ray scattering factor; *f_e(s)* is the electron scattering factor; and *s* = 1/*d* is the resolution. Adding the position-independent, isotropic atomic *B*-factor gives:

$$f_{e,B}(s) = c \frac{Z - f_X(s)}{s^2} e^{-\frac{Bs^2}{4}}$$

This formula is valid if the centre of electron density coincides with the position of the nucleus. If this is not the case, the formula should be modified according to the vector Δx between the centre of electron density and the nuclear position (assuming that the centre of electron density is at the origin):

$$f_{e,B}(s) = c \frac{Ze^{-2\pi s \Delta x} - f_X(s)}{s^2} e^{-\frac{Bs^2}{4}}$$

Note that, in general, the form factor for electron scattering becomes a complex quantity. For all non-hydrogen atoms, it is safe to assume that the centre of electron density and the nuclear position coincide.

For hydrogen atoms, the centre of electron density and the nuclear position do not coincide and we are interested in the peak height for the density of electrostatic potential along the bond between a hydrogen and its parent atom. The formula below ignores the fact that electron densities will be non-spherical, as they are elongated along the bond, thus adding additional complexity to the Mott–Bethe formula.

The densities for the proton and the electron of a hydrogen atom at a resolution *s_{max}* and with a given *B* value is given by:

$$\psi_p(x) = c \int_{|s| < s_{\max}} \frac{Z}{s^2} e^{-\frac{Bs^2}{4}} e^{-2\pi s x} ds = 4\pi Z c \int_0^{s_{\max}} e^{-\frac{Bs^2}{4}} \frac{\sin(2\pi|s||x|)}{2\pi|s||x|} d|s|,$$

$$\psi_e(x) = 4\pi c \int_0^{s_{\max}} f_X(s) e^{-\frac{Bs^2}{4}} \frac{\sin(2\pi|s||x|)}{2\pi|s||x|} d|s|$$

To calculate the density at a position *x* we need to calculate:

$$\psi_{p+e}(x) = \psi_p(x - \Delta x) - \psi_e(x)$$

Even if both densities corresponding to the proton and the electron are spherically symmetric, the combined density will not be spherical. Extended Data Fig. 5 shows density profiles and their maxima for a hydrogen bonded to a carbon atom for different resolutions and *B* values. These profiles were calculated with the assumption that the electron–carbon distance is 0.98 Å and the proton–carbon distance is 1.09 Å.

Reporting summary

Further information on research design is available in the Nature Research Reporting Summary linked to this paper.

Data availability

Atomic coordinates for the GABA_AR construct and apoferritin have been deposited in the Protein Data Bank with accession codes 7A5V and 7A4M, and the cryo-EM density maps have been deposited in the Electron Microscopy Data Bank with accession codes EMD-11657 and EMD-11638, respectively. Raw movies of all datasets have been deposited in the Electron Microscopy Public Image Archive (<https://www.ebi.ac.uk/emdb/>).

Article

ac.uk/pdbe/emdb/empiar/) with accession codes EMPIAR-10500 for GABA_AR and EMPIAR-10424 for apoferritin.

Code availability

Both the implementation of reading EER movies into RELION and the EERformat itself have been distributed as free, open-source software, with downloads available from <https://github.com/3dem/relion> and <https://github.com/fei-company/EerReaderLib>. The in-house-generated Linux port of the BoxNet2D neural network in Warp is available from <https://gist.github.com/biochem-fan/76ff5934495585da56ab2c0af4fe2563>.

35. McMullan, G., Chen, S., Henderson, R. & Faruqi, A. R. Detective quantum efficiency of electron area detectors in electron microscopy. *Ultramicroscopy* **109**, 1126–1143 (2009).
36. Zheng, S. Q. et al. MotionCor2: anisotropic correction of beam-induced motion for improved cryo-electron microscopy. *Nat. Methods* **14**, 331–332 (2017).
37. Mastronarde, D. N. & Held, S. R. Automated tilt series alignment and tomographic reconstruction in IMOD. *J. Struct. Biol.* **197**, 102–113 (2017).
38. Rohou, A. & Grigorieff, N. CTFFIND4: fast and accurate defocus estimation from electron micrographs. *J. Struct. Biol.* **192**, 216–221 (2015).
39. DeRosier, D. J. Correction of high-resolution data for curvature of the Ewald sphere. *Ultramicroscopy* **81**, 83–98 (2000).
40. Tegunov, D. & Cramer, P. Real-time cryo-electron microscopy data preprocessing with Warp. *Nat. Methods* **16**, 1146–1152 (2019).
41. Casañal, A., Lohkamp, B. & Emsley, P. Current developments in Coot for macromolecular model building of electron cryo-microscopy and crystallographic data. *Protein Sci.* **29**, 1055–1064 (2020).
42. Afonine, P. V. et al. Real-space refinement in PHENIX for cryo-EM and crystallography. *Acta Crystallogr.* **74**, 531–544 (2018).
43. Williams, C. J. et al. MolProbity: more and better reference data for improved all-atom structure validation. *Protein Sci.* **27**, 293–315 (2018).
44. Goddard, T. D. et al. UCSF ChimeraX: meeting modern challenges in visualization and analysis. *Protein Sci.* **27**, 14–25 (2018).

Acknowledgements We thank M. van Beers, M. Veerhoek and R. Jonkers for maintaining the Titan Krios microscopes; W. van Dijk, B. van de Kerkhof, S. Konings and G. van Duinen for advice on optics and microscope alignments; B. van Knippenberg, A. Voigt and F. Grollios for support with EPU software; H. Yanagisawa from the Kikkawa laboratory for the apoferritin sample; P. Miller for the GABA_A expression vectors; K. Yamashita for atomic model refinement; A. Koh, T. Darling and J. Grimmett for support with computing; G. Lezcano Singla and E. Franken for support with the EER format; G. van Hoften and G. Hosmar for support with the Falcon-4 camera; and E. Ioannou for logistics support. This work was supported by the EM facilities at the MRC-LMB, the Biochemistry Department of Cambridge University and Thermo Fisher Scientific. The Cryo-EM Facility at Department of Biochemistry is funded by the Wellcome Trust (206171/Z/17/Z; 202905/Z/16/Z) and the University of Cambridge. We acknowledge funding from the UK Medical Research Council (MC_UP_A025_1012 to G. Murshudov, MR/L009609/1 and MC_UP_1201/15 to A.R.A. and MC_UP_A025_1013 to S.H.W.S.); the Japan Society for the Promotion of Science (Overseas Research Fellowship to T.N.); MRC-LMB, Cambridge Trust and School of Clinical Medicine, University of Cambridge (LMB Cambridge Scholarship and Cambridge MB/PhD fellowship to A.S.); the European Commission (Marie Skłodowska-Curie Actions H2020-MSCA-IF-2015/709054 to L.M. and H2020-MSCA-IF-2017/793653 to P.M.G.E.B.); EMBO (long term fellowship 300-2015 to L.M.); Cancer Research UK (T.M., grants C20724/A14414 and C20724/A26752 to C. Siebold, University of Oxford); Boehringer Ingelheim Fonds (PhD Fellowship to J. Miehling; and the Research Foundation – Flanders (FWO, PhD Fellowship to T.U.).

Author contributions E.d.J., J.K., M.B., J. McCormack and P.T. contributed to microscope hardware and software developments; G. McMullan performed DQE analysis; D.K., A.S. and S.M. prepared cryo-EM grids; T.U. produced megabodies; A.K., L.Y., E.V.P., S.W.H. and D.Y.C. acquired cryo-EM data; T.N., A.K., A.S., L.Y., S.M., P.M.G.E.B., I.T.G., L.M., J. Miehling and S.H.W.S. analysed cryo-EM data; T.N., A.R.A., T.M. and G. Murshudov prepared atomic models; T.N., A.K., A.R.A. and S.H.W.S. conceived the project and designed the experiments; G.M., A.R.A. and S.H.W.S. wrote the manuscript, with input from all authors.

Competing interests A.K., S.M., L.Y., D.K., E.V.P., E.d.J., J.K., M.B., J. McCormack and P.T. are employees of Thermo Fisher Scientific. The other authors declare no competing interests.

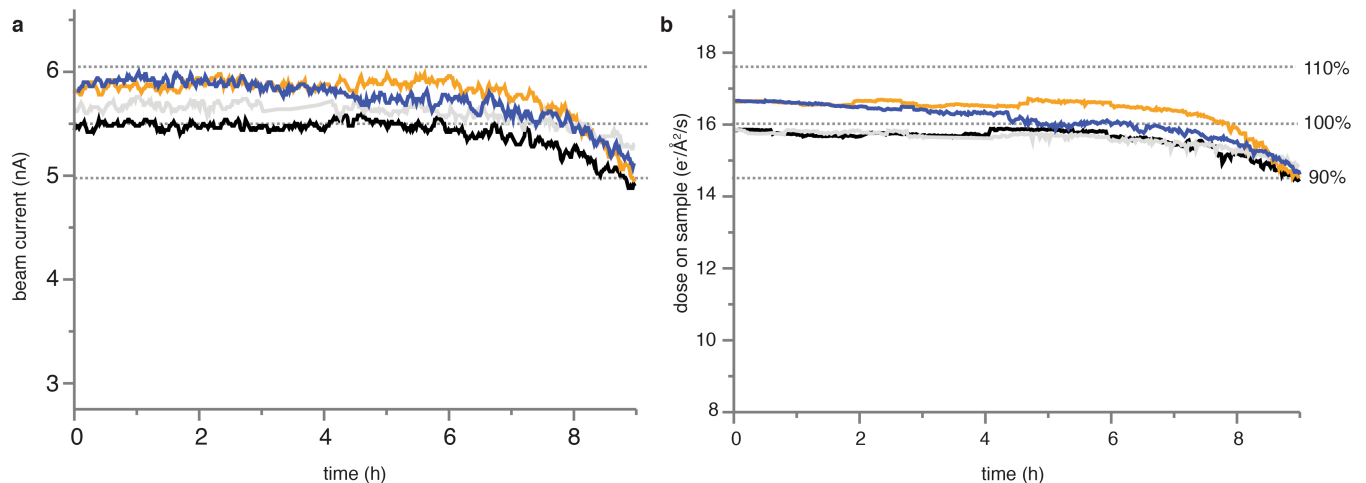
Additional information

Supplementary information is available for this paper at <https://doi.org/10.1038/s41586-020-2829-0>.

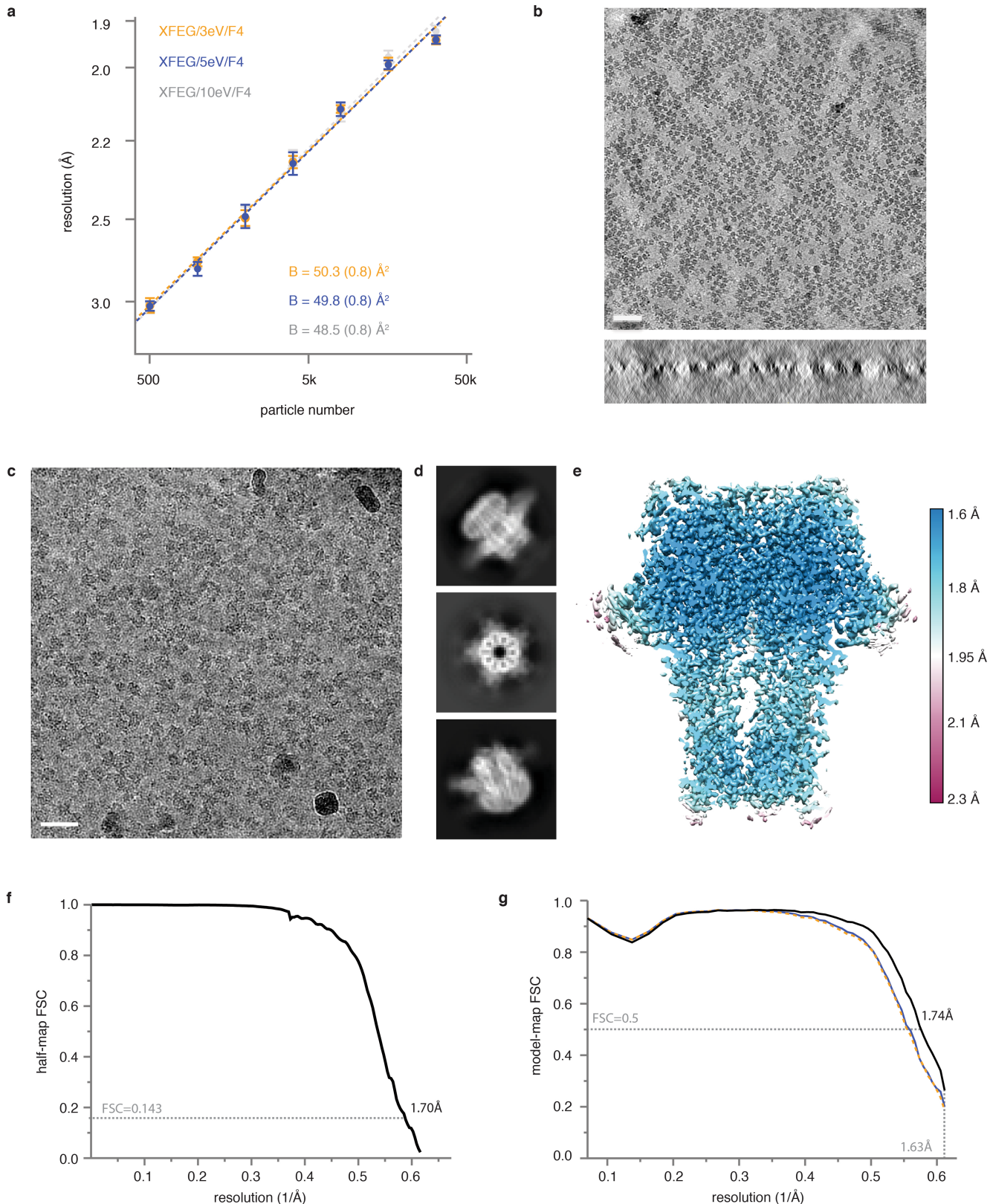
Correspondence and requests for materials should be addressed to A.R.A. or S.H.W.S.

Peer review information *Nature* thanks Serban Ilca, Henning Stahlberg and the other, anonymous, reviewer(s) for their contribution to the peer review of this work. Peer reviewer reports are available.

Reprints and permissions information is available at <http://www.nature.com/reprints>.

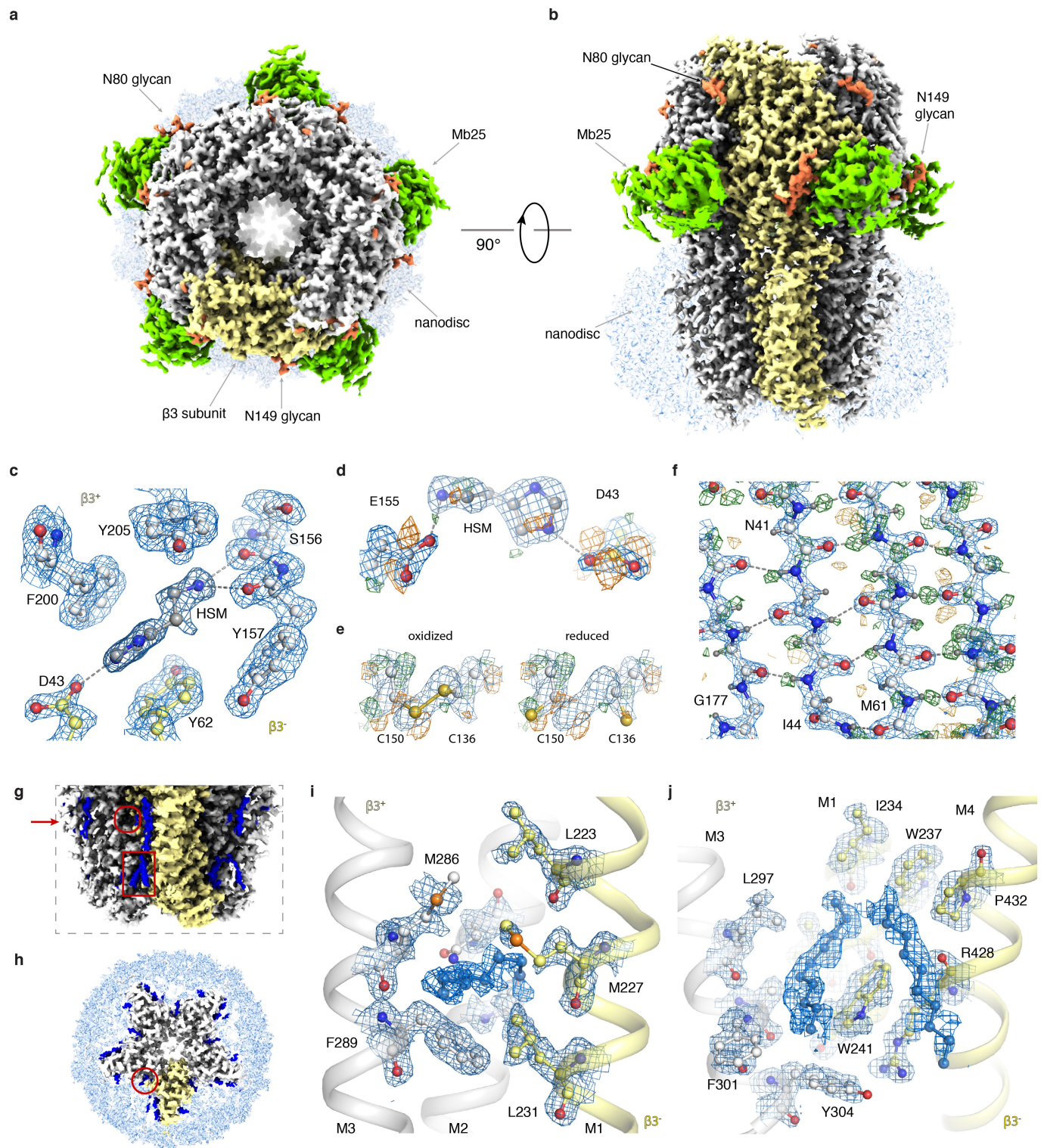


Extended Data Fig. 1 | Characteristics of the new cryo-EM technology. **a**, Four consecutive measurements of the CFEG beam current over a period of nine hours. The FEG tip was flashed just before the start of each measurement. **b**, The dose at the sample as measured for the same four experiments in **a**.



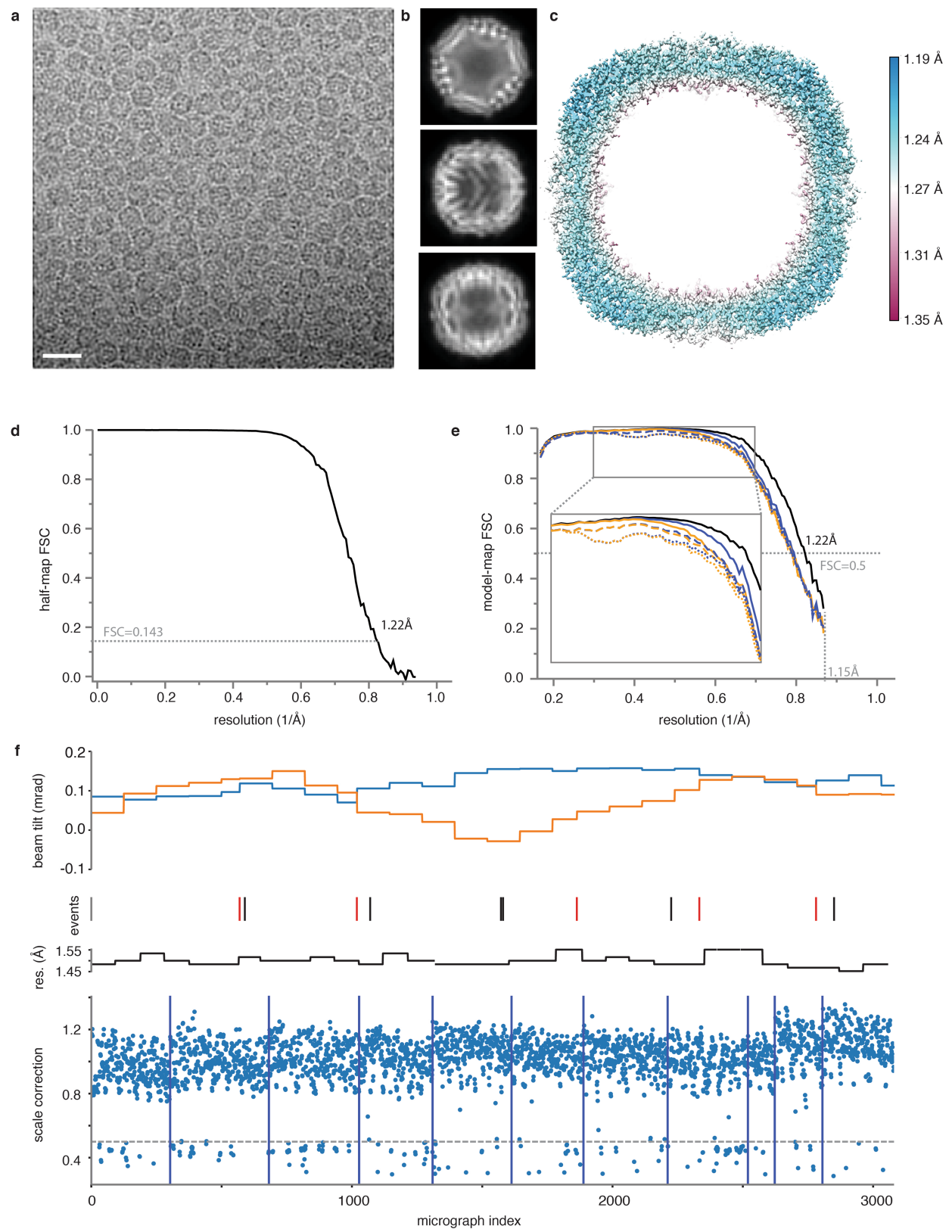
Extended Data Fig. 2 | Cryo-EM for GABA_AR. **a**, B-factor plots for three datasets using an X-FEG, the new energy filter with a slit width of 3eV (orange), 5eV (blue) and 10 eV (grey) and a Falcon-4 camera. **b**, Two orthogonal views of an electron tomogram for ice thickness measurement. Scale bar is 50 nm. **c**, Representative electron micrograph from the CFEG dataset. Scale bar is 30 nm. **d**, A selection of 2D class average images. **e**, Local resolution map.

f, Fourier Shell Correlation (FSC) between the two independently refined half-maps. **g**, FSC between the model and the map calculated for the model refined against the full reconstruction (black); the model refined in the first half-map against that half-map (FSC_{work} ; blue); and the model refined in the first half-map against the second half-map (FSC_{test} ; dashed orange). Atomic models were refined including spatial frequencies up to 1.63 Å.



Extended Data Fig. 3 | GABA_AR reconstruction details. **a**, The GABA_AR cryo-EM map viewed from the extracellular space (top view). The density of one subunit of the homopentamer is highlighted in yellow; glycans are orange; the nanobody domain of Mb25 green; and the lipid nanodisc light blue. **b**, As in **a**, but viewed parallel to the plasma membrane space (side view). **c**, Stacking of histamine with aromatic residues in the ligand-binding pocket. Water molecules removed for clarity. **d**, Radiation damage in the ligand-binding pocket illustrated by difference maps of Asp43 and Glu155 carboxyl groups. **e**, Radiation damage causes partial reduction of the disulfide bond between Cys136 and Cys150. Left panel: oxidized state, right panel: reduced state. Only Cα, Cβ and sulfur atoms depicted for clarity. **f**, Difference map revealing the

hydrogen bonding network between β-strands. **g**, A close-up view of the lipids (blue) surrounding the transmembrane region of the receptor. Compared to **a**, **b**, the contour level is decreased. Red arrow indicates section level as depicted in **h**. The general anaesthetics pocket and the neurosteroid modulation site are indicated by the red circle and rectangle, respectively. **h**, Top-view of a transverse section through the GABA_AR transmembrane region shows semi-ordered lipids surrounding individual subunits. **i**, Close-up view of the general anaesthetics pocket. **j**, Close-up view of the neurosteroid modulation site. Lipids in **i** and **j** could not be identified unambiguously and therefore are modelled as aliphatic chains.

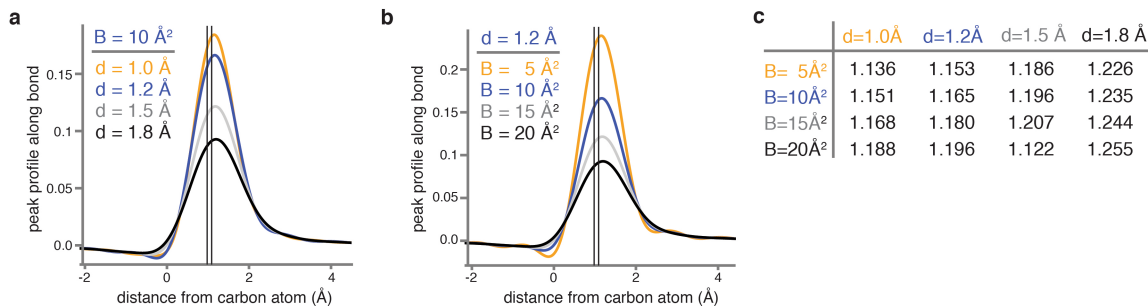


Extended Data Fig. 4 | See next page for caption.

Extended Data Fig. 4 | Cryo-EM for apoferritin. **a**, Representative electron micrograph. Scale bar is 20 nm. **b**, 2D class average images. **c**, Local resolution map. **d**, Fourier Shell Correlation (FSC) between the two independently refined half-maps. **e**, FSC between the model and the map as calculated for the model refined against the full reconstruction against that map (black); the model refined in the first half-map against that half-map (FSC_{work} ; blue); and the model refined in the first half-map against the second half-map (FSC_{test} ; dashed orange). FSC_{work} and FSC_{test} curves are shown for three different models: with hydrogens and anisotropic B-factors (solid lines); with hydrogens and isotropic B-factors (dashed lines); and without hydrogens and with isotropic B-factors

(dotted lines). Including hydrogens and using anisotropic B-factors gives a better fit to the data at medium resolution, but lead to a small amount of overfitting at high resolution. Atomic models were refined including spatial frequencies up to 1.15 Å. **f**, The beam tilt in X (blue) and Y (orange); the resolution (res.) for subsets of 5,000 consecutive particles (black); and RELION's rlnGroupScaleCorrection values for individual micrographs (blue dots) during the data acquisition experiment. Events like CFEG flashing (red), liquid nitrogen filling (black) and moving the grid to another grid square (dark blue) are indicated with vertical lines. The cutoff in scale correction values used to discard part of the micrographs is indicated with a dashed grey line.

Article



Extended Data Fig. 5 | Electrostatic potential of hydrogen atoms.

a, Calculated profile (see Methods) of the electrostatic scattering potential along the bond between a carbon and a hydrogen atom, for a B -value of 10 \AA^2 and resolutions (d) of 1.0 \AA (orange), 1.2 \AA (blue), 1.5 \AA (grey) and 1.8 \AA (black). The two vertical lines indicate the electron-carbon distance of 0.98 \AA and the

proton-carbon distance of 1.09 \AA . **b**, As in **a**, but for a resolution of 1.2 \AA and B -values of 5 \AA^2 , 10 \AA^2 , 15 \AA^2 and 20 \AA^2 . **c**, Distances from the carbon atom (in \AA) at which the calculated profile of the electrostatic scattering potential along the bond between a carbon and a hydrogen atom is at its maximum, for different resolutions (d) and B -values.

Extended Data Table 1 | Cryo-EM data collection parameters

	Apoferritin	GABA _A -β3						
Data collection and processing								
Electron Gun Detector	CFEG Falcon4	CFEG Falcon4	XFEG BM-Falcon3	XFEG K3				
Magnification	270k	165k	165k	165k	165k	165k	96k	130k
Energy filter slit width (eV)	10	5	open	10	5	3	NA	20
Voltage (kV)	300	300	300	300	300	300	300	300
Flux on detector (e-/pix/sec)	4.5	4.7	2.7	2.8	2.8	2.8	0.7	14.9
Electron exposure on sample (e-/Å ²)	40	40	35	35	35	35	37	40
Target defocus range (μm)	0.3-0.9	0.3-1.1	0.9-1.8	0.3-1.1	0.3-1.1	0.3-1.1	0.5-1.5	0.3-1.5
Observed defocus range (95th percentile in μm)	0.27-0.97	0.30-1.11	0.80-1.83	0.31-0.95	0.32-0.87	0.34-1.00	0.58-1.51	0.48-1.46
Calibrated pixel size (Å)	0.457	0.727	0.735	0.735	0.735	0.735	0.827	0.65482
Symmetry imposed	O	C5						
Number of collected movies	3370	8733	1244	1268	1556	1952	1501	1507
Initial particle images (no.)	428590	1105069	192053	199867	242059	264675	412913	215957
Final particle images (no.)	363126	233576	33166	42780	45009	50328	129810	46441
Map resolution at FSC=0.143 (Å)	1.22	1.73	1.97	1.89	1.87	1.88	1.97	2.32

Article

Extended Data Table 2 | Refinement and validation statistics

Refinement	Apo ferritin (EMD-11638) (PDB 7A4M) (EMPIAR- 10424)	GABA _A -β3 (EMD-11657) (PDB 7A5V) (EMPIAR- 10500)
Map resolution range refined against (Å)	1.22 - 136.5	1.6 - 291.1
Map sharpening <i>B</i> factor (Å ²)	2.3	23
Model composition in the asymmetric unit		
Protein residues	189	480
Non-hydrogen atoms	1668	4231
Protein atoms	1556	3850
Waters	110	204
Ions	2	2
Glycans	-	103
HSM	-	8
Lipids	-	64
Isotropic <i>B</i> factors (Å ²)		
Protein	23.3	51.2
Waters	36.2	45.7
Ions	26.6	67.2
Glycans		79.1
HSM	-	28.1
Lipids	-	110.0
R.m.s. deviations		
Bond lengths (Å)	0.009	0.009
Bond angles (°)	1.549	1.300
Validation		
MolProbity score	1.10	1.10
Clashscore	2.61	2.32
Poor rotamers (%)	1.18	0.48
Ramachandran plot		
Favored (%)	98.24	97.56
Allowed (%)	1.76	2.44
Outliers (%)	0.00	0.00

Reporting Summary

Nature Research wishes to improve the reproducibility of the work that we publish. This form provides structure for consistency and transparency in reporting. For further information on Nature Research policies, see our [Editorial Policies](#) and the [Editorial Policy Checklist](#).

Statistics

For all statistical analyses, confirm that the following items are present in the figure legend, table legend, main text, or Methods section.

n/a Confirmed

- The exact sample size (n) for each experimental group/condition, given as a discrete number and unit of measurement
- A statement on whether measurements were taken from distinct samples or whether the same sample was measured repeatedly
- The statistical test(s) used AND whether they are one- or two-sided
Only common tests should be described solely by name; describe more complex techniques in the Methods section.
- A description of all covariates tested
- A description of any assumptions or corrections, such as tests of normality and adjustment for multiple comparisons
- A full description of the statistical parameters including central tendency (e.g. means) or other basic estimates (e.g. regression coefficient) AND variation (e.g. standard deviation) or associated estimates of uncertainty (e.g. confidence intervals)
- For null hypothesis testing, the test statistic (e.g. F , t , r) with confidence intervals, effect sizes, degrees of freedom and P value noted
Give P values as exact values whenever suitable.
- For Bayesian analysis, information on the choice of priors and Markov chain Monte Carlo settings
- For hierarchical and complex designs, identification of the appropriate level for tests and full reporting of outcomes
- Estimates of effect sizes (e.g. Cohen's d , Pearson's r), indicating how they were calculated

Our web collection on [statistics for biologists](#) contains articles on many of the points above.

Software and code

Policy information about [availability of computer code](#)

Data collection EPU v2.5 (Thermo Fisher Scientific)

Data analysis RELION v3.1 (<https://github.com/3dem/relion>), EER reader (<https://github.com/fei-company/EerReaderLib>), CTFFIND-4.1.13, COOT v0.9-pre, REFMAC v5.8.0258, PHENIX version 1.16.3549 and v1.17.1, Pymol v1.8.4, UCSF ChimeraX v1.0, MolProbity, IMOD 4.10, Warp v1.06, in-house generated Linux port of the BoxNet2D neural network in Warp (available from <https://gist.github.com/biochem-fan/76ff5934495585da56ab2c0af4fe2563>)

For manuscripts utilizing custom algorithms or software that are central to the research but not yet described in published literature, software must be made available to editors and reviewers. We strongly encourage code deposition in a community repository (e.g. GitHub). See the Nature Research [guidelines for submitting code & software](#) for further information.

Data

Policy information about [availability of data](#)

All manuscripts must include a [data availability statement](#). This statement should provide the following information, where applicable:

- Accession codes, unique identifiers, or web links for publicly available datasets
- A list of figures that have associated raw data
- A description of any restrictions on data availability

Atomic coordinates for the GABAAR construct and apo-ferritin have been deposited in the Protein Data Bank with accession codes 7A5V and 7A4M and the cryo-EM density maps have been deposited in the Electron Microscopy Data Bank with accession codes EMD-11657 and EMD-11638, respectively. Raw movies of all datasets have been deposited in the Electron Microscopy Public Image Archive with accession codes EMPIAR-10500 for GABAAR and EMPIAR-10424 for apo-ferritin.

Field-specific reporting

Please select the one below that is the best fit for your research. If you are not sure, read the appropriate sections before making your selection.

Life sciences Behavioural & social sciences Ecological, evolutionary & environmental sciences

For a reference copy of the document with all sections, see nature.com/documents/nr-reporting-summary-flat.pdf

Life sciences study design

All studies must disclose on these points even when the disclosure is negative.

Sample size	No statistical method was used to determine sample size. Sample sizes were determined by available electron microscopy time and the number of particles on electron microscopy grids. The sample size is sufficient to obtain a structure at the reported resolution, as assessed by Fourier shell correlation.
Data exclusions	Micrographs whose estimated resolution from CTFFIND was worse than 5 Å were removed (rlnCtfMaxResolution). Pre-established common image classification procedures (S.H.W. Scheres, J. Struc. Biol. 180: 519–530, (2012)) were employed to select particle images with the highest resolution content in the cryo-EM reconstruction process. Micrographs with refined scale factors (rlnGroupScaleCorrection) with values below 0.5 were also removed. Details of the number of selected images are given in Supplemental Data Table 1.
Replication	Two independent maps were refined for both apoferritin and GABAA in order to estimate resolution according to the recommended procedures in the field (the 'gold standard').
Randomization	Division of datasets into two random halves was done based on standard approach in RELION 3.1.
Blinding	Blinding was not applicable to this study because this type of study does not use group allocation.

Reporting for specific materials, systems and methods

We require information from authors about some types of materials, experimental systems and methods used in many studies. Here, indicate whether each material, system or method listed is relevant to your study. If you are not sure if a list item applies to your research, read the appropriate section before selecting a response.

Materials & experimental systems		Methods	
n/a	Involved in the study	n/a	Involved in the study
<input type="checkbox"/>	<input checked="" type="checkbox"/> Antibodies	<input checked="" type="checkbox"/>	<input type="checkbox"/> ChIP-seq
<input type="checkbox"/>	<input checked="" type="checkbox"/> Eukaryotic cell lines	<input checked="" type="checkbox"/>	<input type="checkbox"/> Flow cytometry
<input checked="" type="checkbox"/>	<input type="checkbox"/> Palaeontology and archaeology	<input checked="" type="checkbox"/>	<input type="checkbox"/> MRI-based neuroimaging
<input checked="" type="checkbox"/>	<input type="checkbox"/> Animals and other organisms		
<input checked="" type="checkbox"/>	<input type="checkbox"/> Human research participants		
<input checked="" type="checkbox"/>	<input type="checkbox"/> Clinical data		
<input checked="" type="checkbox"/>	<input type="checkbox"/> Dual use research of concern		

Antibodies

Antibodies used	High Capacity Streptavidin Agarose Resin was purchased from Thermo Scientific. Rho-1D4 antibody was purchased from the University of British Columbia. The megabody Mb25 is available upon request.
Validation	The nanobody Nb25, used to design the megabody Mb25 as described in methods, was characterised and published elsewhere (PMID: 28991263). Mb25 has been characterised and published elsewhere (https://www.biorxiv.org/content/10.1101/812230v1.full.pdf).

Eukaryotic cell lines

Policy information about cell lines	
Cell line source(s)	HEK 293S GnT-I- cells were obtained from ATCC.
Authentication	Further authentication was not performed for this study.
Mycoplasma contamination	Mycoplasma testing was not performed for this study.

Commonly misidentified lines
(See [ICLAC](#) register)

No commonly misidentified cell lines were used in this study.